

DOES NEARBY OPEN FLUX AFFECT THE ERUPTIVITY OF SOLAR ACTIVE REGIONS?

MARC L. DEROSA¹ AND GRAHAM BARNES²

¹*Lockheed Martin Solar and Astrophysics Laboratory, 3251 Hanover St. B/252, Palo Alto, CA 94304, USA*

²*NorthWest Research Associates, 3380 Mitchell Ln., Boulder, CO 80301, USA*

ABSTRACT

The most energetic solar flares are typically associated with the ejection of a cloud of coronal material into the heliosphere in the form of a coronal mass ejection (CME). However, there exist large flares which are not accompanied by a CME. The existence of these non-eruptive flares raises the question of whether such flares suffer from a lack of access to nearby open fields in the vicinity above the flare (reconnection) site. In this study, we use a sample of 56 flares from Sunspot Cycles 23 and 24 to test whether active regions that produce eruptive X-class flares are preferentially located near coronal magnetic field domains that are open to the heliosphere, as inferred from a potential field source surface model. The study shows that X-class flares having access to open fields are eruptive at a higher rate than those for which access is lacking. The significance of this result should be moderated due to the small number of non-eruptive X-class flares in the sample, based on the associated Bayes factor.

Keywords: Sun: corona — Sun: flares — Sun: magnetic fields — Sun: coronal mass ejections (CMEs)

1. INTRODUCTION

The Sun is an active star that possesses a continually evolving, magnetized corona. The continuous, quasi-steady evolution that is observed to occur most of the time is occasionally interrupted by solar flares, which represent the very rapid conversion of built-up magnetic free energy into light, heat, and kinetic motions on time scales of about a few minutes.

The magnetic energy conversion occurs via magnetic reconnection, which is assumed to take place in a thin layer of the corona where the Ohmic resistivity is high enough to facilitate the transfer of energy from the field to the plasma. Understanding the detailed dynamics of both the reconnection region and how flares are triggered are areas of active research (see, e.g., the recent review by [Janvier 2017](#) and references therein).

Theoretical treatments indicate that reconnection is more likely to occur at particular locations in the magnetic field topology, such as null points, separatrix surfaces, and quasi-separatrix layers (as reviewed by, e.g., [Pontin 2012](#)). Determining the locations of such topologically important features in the solar corona is challenging, however, owing to the lack of direct measurements of the coronal magnetic field on the spatial scales needed to discern these features. Although the coronal field topology is often more evident from observations off the solar limb (e.g., [Lin et al. 2004](#)), the complementary photospheric magnetic field observations needed for proper interpretation of the observed limb structures are compromised by foreshortening.

In practice, indirect measurements of coronal magnetic field topology, typically inferred using some combination of coronal imagery and coronal field modeling, are used. Such indirect methods have been used to investigate a broad range of properties, including the persistence of bright loop fans surrounding active regions (ARs) that are otherwise quiescent ([Schrijver et al. 2010](#)); how open flux maps down to the photosphere ([Antiochos et al. 2011; Platten et al. 2014](#)); cusps in coronal limb observations ([Freed et al. 2015](#)); flare ribbon geometries and evolution ([Zhao et al. 2014, 2016; Pontin et al. 2016](#)); the temporal concurrence of spatially separated events, including “sympathetic flares” ([Schrijver & Title 2011; Jin et al. 2016](#)); how the solar wind may be related to AR upflows in regions of apparently closed fields ([Edwards et al. 2016](#)); and why the composition of the solar wind near the boundaries between open and closed field appears to be a mixture of plasma from both open and closed regions ([Pontin & Wyper 2015](#)).

Solar flares are most often characterized by their emission in X-ray wavelengths, as detected by the X-ray spectrometers on board the various *Geostationary Orbiting Environmental Satellite* (GOES) missions over the years, operated by the U.S. National Oceanic and Atmospheric Administra-

tion (NOAA). The GOES flare catalog¹ categorizes flares in terms of their peak flux in the 1–8 Å wavelength band. The strongest and brightest flares, X-class flares, have a peak flux in the 1–8 Å band of at least 10^{-4} W m⁻² and are often associated with coronal mass ejections (CMEs), in which a cloud of coronal material is observed to be accelerated upward against gravity, away from the Sun, and into the heliosphere. Although there is some correlation between the X-ray emission of flares in the GOES catalog and the properties and characteristics (e.g., ejection velocities) of the ensuing CMEs, direct proportionality should not be assumed ([Emslie et al. 2012](#)). It is thus important to keep in mind that the peak X-ray emission from a flare is not necessarily a good indicator of the total energy involved in the reconnection process.

Indeed, some X-class flares are not followed by any discernible eruption, such as SOL2011-11-03T20:27 from NOAA AR 11339 ([Liu et al. 2014](#)) and the cluster of X-class flares from AR 12192 in October of 2014 ([Sun et al. 2015](#)). An understanding of why most X-class flares are accompanied by CMEs, but some are not, probably depends on detailed knowledge of the forces responsible for the upward acceleration of the coronal material at the core of the flaring AR, how these forces compare to the downward forces that confine this material in the lower corona, and the partitioning of energy resulting from the reconnection process.

The scenario in which an X-class flare is not followed by any noticeable eruption is intriguing. For the majority of X-class flares, the large amount of energy associated with the X-ray emission is usually accompanied by enough additional energy to overcome the confining forces and accelerate coronal plasma into the heliosphere. The existence of non-eruptive flares, however, raises the question of whether such flares suffer from a lack of access to nearby open fields above the flare (reconnection) site in which overlying closed fields effectively block the upward rise of lower-lying flux structures. The observational and numerical studies by [Toriumi et al. \(2017\)](#) and ([Toriumi & Takasao 2017](#)) show that the ratio between the amount of flux involved in the reconnection process and the total AR flux is smaller for non-eruptive flares than for eruptive flares, supporting this possibility. A related study by [Wang et al. \(2017\)](#) also indicates a propensity for the large-scale coronal field associated with non-eruptive flaring ARs to be more confining.

If the hypothesis presented above is true, then one would expect a decreased likelihood of eruptivity in cases where the flaring AR is buried more deeply underneath a significant amount of closed magnetic fields. Stated more broadly, identifying whether the presence or absence of particular topological features in the large-scale coronal magnetic field is

¹ At the time of this writing, yearly lists of GOES flares dating back to September 1975 can be downloaded at <https://www.ngdc.noaa.gov/stp/space-weather/solar-data/solar-features/solar-flares/x-rays/goes/xrs/>.

correlated with whether a flare is confined or eruptive may be a useful diagnostic of the propensity of a flaring AR to foster an eruption.

In the study presented here, we investigate whether the nature of the coronal fields that lie above the locations of strong flares is a contributing factor in determining whether these flares are accompanied by plasma ejected into the heliosphere. More specifically, we test the hypothesis that ARs in which eruptive flares occur are preferentially located near open fields, and conversely that ARs in which confined flares occur are preferentially located underneath closed topological structures. To perform this test, we apply topological analysis software to models of the global coronal magnetic field corresponding to the times of 56 X-class flares in the GOES flare catalog from the past two decades spanning sunspot Cycles 23 and 24. Using statistical methods, we estimate the rate at which flares from ARs with access to open field are eruptive and compare this estimate to the rate from ARs under closed field.

2. METHODOLOGY

2.1. *Obtaining the Flare Sample*

According to the GOES database, 176 X-class flares have occurred since the beginning of sunspot Cycle 23 in 1996.² The large-scale magnetic environment surrounding each flaring AR may be assessed using models of the global solar coronal magnetic field, including the oft-used potential field source-surface (PFSS) model used in this study.

Determining the magnetic environment associated with each flare location presupposes that the flare location is known. However, some X-class flares in the GOES database from sunspot Cycles 23 and 24 have indeterminate locations, which unfortunately results in their removal from the sample unless the location of the AR can be determined by other means. During sunspot Cycle 23, the absence of H-alpha images contemporaneous with the flares is a significant factor in the lack of locational knowledge. During sunspot Cycle 24 all flares on disk can be determined using the frequent imagery from the Atmospheric Imaging Assembly (AIA; Lemen et al. 2012) instrument on the Solar Dynamics Observatory (SDO). Flares at the limb suffer from the issue of geometrical foreshortening that makes determinations of precise longitudes difficult.

The PFSS approximation assumes that the coronal volume is current-free, enabling the magnetic field within a spheri-

cal shell to be calculated given full-Sun magnetic maps of the photosphere (Schatten et al. 1969). The boundary conditions are completely specified if it is also assumed that the magnetic field is purely radial at the upper boundary. In this study, the lower boundary at $R_{\text{bot}} = R_{\odot}$ in the PFSS models are provided by sampling the evolving flux-transport model of Schrijver & DeRosa (2003), in which magnetograms from either the Michelson Doppler Imager (MDI; Scherrer et al. 1995) on board the Solar and Heliospheric Observatory (SOHO) spacecraft (between 1996 and 2010) or the Helioseismic and Magnetic Imager (HMI; Schou et al. 2012) on board SDO (after 2010) are incorporated into the model. The radius of the upper boundary is chosen to be the canonical value of $R_{\text{top}} = 2.5R_{\odot}$. Both such models used here, namely the evolving surface-flux models of the photospheric magnetic field and the subsequent PFSS models of the coronal magnetic field, are publicly available for download via the `pfss` package from the SolarSoftWare (SSW) distribution system.

PFSS models are affected by the additional issue that new flux is only incorporated into the model after it appears in MDI or HMI magnetograms. Occasionally, an AR located at or near the east limb that contains a significant amount of flux and that is not yet incorporated into the model does affect the arrangement of coronal magnetic fields at on-disk longitudes (as explored in, e.g., Nitta & DeRosa 2008 or Schrijver & Title 2011). In the more extreme cases, unaccounted east-limb flux may affect the global field situated as far away as 90° to 120° of longitude. We therefore have more confidence in the modeled magnetic fields for locations west of the central meridian (i.e., farther away from possible missing flux on the east limb) than for locations in the eastern hemisphere, and as a result we have screened out all flares with locations east of the central meridian. The final sample comprises 56 flares occurring within 37 ARs, as detailed in Table 1.

2.2. *PFSS Model Sanity Checks*

PFSS models assume a current-free magnetic field solution, and thus these models are not physically appropriate in the low corona in the cores of ARs, where significant currents are known to exist. However, farther away from ARs, PFSS models often possess field geometries that resemble many larger-scale features observed in the solar coronal magnetic field, suggesting that much of the coronal volume is largely current-free. Because this investigation considers only coronal magnetic fields on larger spatial scales, PFSS models are assumed appropriate; it nonetheless seems prudent to evaluate the resemblance between observations and the PFSS models for the specific times considered here to see whether there are any significant discrepancies, as a sanity check.

To this end, we employ two qualitative tests: (1) comparisons between the topological structures found in PFSS models with the locations of streamers and pseudostreamers evident in white-light coronagraph images, and (2) com-

² The following query to the Heliophysics Events Knowledgebase (Hurlburt et al. 2012) yields the full list of GOES X-class flares occurring between 1996 and 2017: https://www.lmsal.com/isolsearch?hek_query=https://www.lmsal.com/hek/her?cosec=2&cmd=search&type=column&event_type=fl&event_starttime=1996-01-01&event_endtime=2018-01-01&event_region=all&event_coordsys=helioprojective&x1=-5000&x2=5000&y1=-5000&y2=5000&result_limit=200&sparam0=FL_GOESC1s&op0=%3E=&value0=X1&sparam1=FRM_Name&op1==&value1=SWPC

parisons between the locations of coronal holes visible in extreme ultraviolet (EUV) images with the open-flux regions determined from the PFSS models. For all events, these tests either support the idea that the coronal magnetic field is current-free on large scales, or were inconclusive. The online materials associated with this article (<http://www.lmsal.com/forecast/DB2018.html>) provide images and topological renderings for each of the 56 events used for this investigation. These images allow the reader to assess the applicability of the PFSS model in the manner described in this section.

Although more rigorous comparison schemes are possible, these involve more physically realistic modeling of the coronal magnetic field. These more rigorous tests are not considered here, as such modeling requires knowledge of (at least) photospheric currents, plasma densities and temperatures, and/or coronal heating mechanisms — quantities that are generally not readily available for a large enough sample of ARs and for a large enough area on the Sun. Additionally, these models are more computationally intensive and are not as readily applied to a large sample of regions.

2.2.1. Comparisons with (Pseudo-)Streamers

The first sanity check is based on the fact that the cusp-shaped streamers evident in white-light coronagraph images from, e.g., the Large Angle and Spectrometric Coronagraph (LASCO; Brueckner et al. 1995) on SOHO result from the increased density associated with tall, high-arching closed fields that underlie the heliospheric current sheet (HCS). If a PFSS model successfully captures the largest spatial scales in the actual coronal field, then the position angles of the LASCO streamers are expected to correspond with the highest-arching closed-field structures in the PFSS model. The persistence of coronal streamers over several rotation periods (an observational fact that was first realized approximately 50 years ago, e.g., Bohlin 1970) lends credence that streamers are a robust feature of the large-scale corona. The magnetic null points associated with these streamers located lower down in the corona have also been found to persist (Freed et al. 2015).

Examples of this first test are demonstrated in Figures 1 and 2, corresponding to the times of Events 11 and 48 in Table 1. In both figures, the topological skeleton associated with the PFSS model nearest to the time of the event is shown in panel (a) and a corresponding LASCO C2 image in panel (b). The topological skeleton renderings shown here are largely similar to those shown in Platten et al. (2014), and illustrate the separatrix surfaces, null points, and spine lines in the PFSS models. These features are depicted in the figures as semi-transparent surfaces, small red dots, and cyan lines, respectively. We note as an aside that the same topological elements of interest found in the PFSS models, such as the location of null points and the boundaries between magnetic field connectivity domains, are likely to also be present in non-potential fields (Régnier 2012). The algorithms by

which the topological features were calculated are the null-point finding method of Haynes & Parnell (2007) and the separatrix-surface mapping scheme described in Haynes & Parnell (2010), after adapting for spherical geometries.

In the comparison with LASCO images, the most relevant topological features in the PFSS models are the separatrix surfaces that intersect R_{top} . The largest and most noticeable separatrix surfaces of this kind are the surfaces that extend downward from the polarity-inversion line at R_{top} , and serve to separate fieldlines that are considered open to the heliosphere (i.e., fieldlines that have one endpoint at R_{bot} and another at R_{top}) from closed fieldlines (i.e., fieldlines having both endpoints at R_{bot}). These *HCS curtains* (as termed by Platten et al. 2014) are colored yellow in Figures 1(a) and 2(a), and the polarity-inversion line at R_{top} at the apexes of these surfaces is colored dark blue. HCS curtains are conceptualized to continue upward to form the HCS (as in Figure 1 of their paper) and to be at the same position angles in the PFSS models, when viewed from along the Earth-Sun line, as the white-light coronal streamers seen in LASCO images (Wang et al. 2007a).

Additionally, each null point located inside PFSS coronal volume has a separatrix surface associated with it. While these surfaces often take the shape of domes that wall off self-contained domains of fieldlines covering sections of the photosphere, in some cases the fan plane extending away from a null point is found to be oriented vertically, such that the associated separatrix surface extends upward and intersects R_{top} . These *separatrix curtains* (as termed by Platten et al. 2014) divide open fieldlines having the same polarity, and are often associated with coronal pseudostreamers observed in the LASCO images (Wang et al. 2007b). In Figures 1(a) and 2(a), all separatrix surfaces associated with coronal nulls (including the separatrix curtains) are rendered in various pastel colors. The intersection of these separatrix surfaces with either the upper or lower boundary are colored red.

Because the HCS curtains and separatrix curtains are both associated with LASCO streamers and pseudostreamers, comparisons between the renderings of the topological skeletons of the PFSS models (centered on the solar central-meridian longitude and latitude for the time of interest) and the LASCO images provide a way to validate the PFSS models. In Figure 1, corresponding to Event 11, the position angles of the three brightest streamers in LASCO (marked by arrows) match well with the HCS curtains and one of the upward-extending separatrix curtains. As a result, the PFSS model for Event 11 is considered plausible.

In Figure 2, corresponding to Event 48, the comparison is less conclusive. The LASCO image contains a multitude of streamers and pseudostreamers. The PFSS model topology is also more complex, with an undulating and warped HCS curtain surrounded by many smaller separatrix curtains. In this case, it is more difficult to predict where streamers might

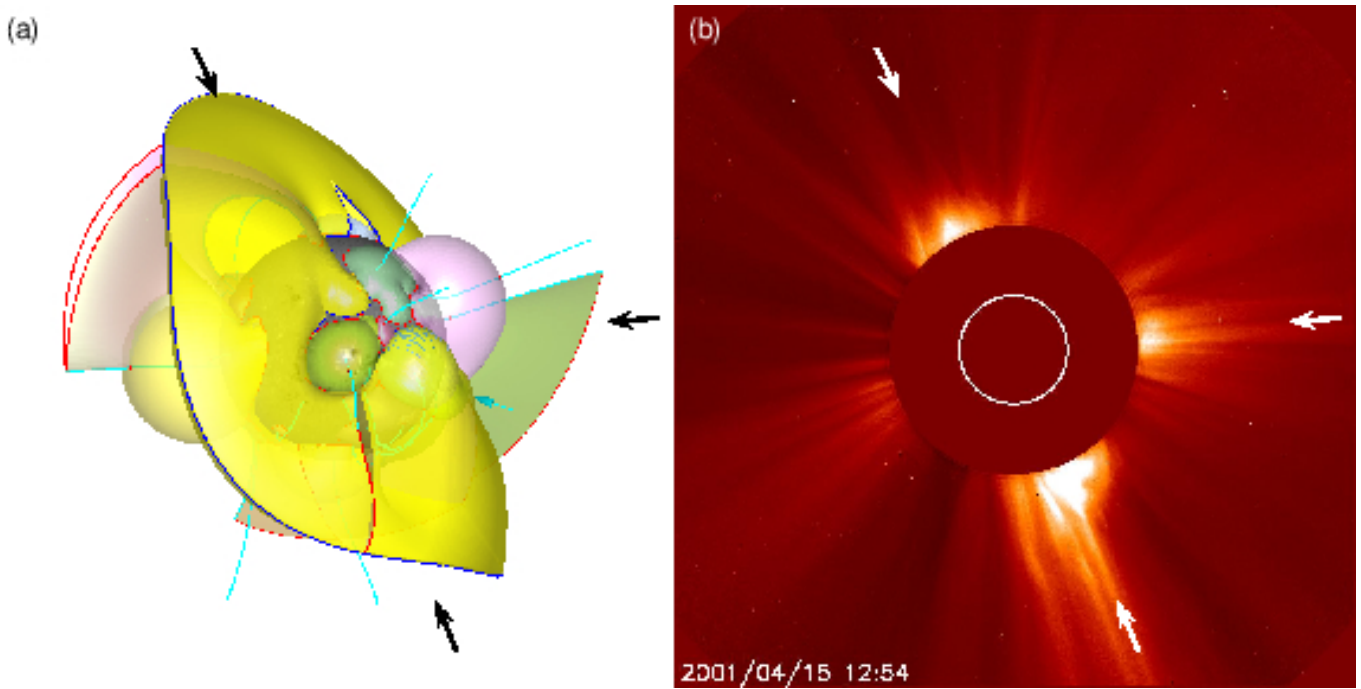


Figure 1. SOL2001-04-15T13:50 (Event 11 in Table 1) comparison: (a) Topological skeleton for the PFSS model of 2001 April 15 at 12:04 UT and (b) the corresponding LASCO C2 image. The topological skeleton comprises the separatrix surfaces (semi-transparent surfaces), null points (small red dots), and spine lines (cyan lines) present in the PFSS model. The dark-blue line is the polarity-inversion line at the upper boundary of the model at $R_{\text{top}} = 2.5R_{\odot}$. Red lines are drawn where the separatrix curtains intersect R_{bot} and R_{top} . The arrows in both images indicate the positions of the brightest LASCO streamers, which correspond to the largest separatrix surfaces in the topology skeleton. The conical cyan pointer indicates the location of the X-class flare at S20W85.

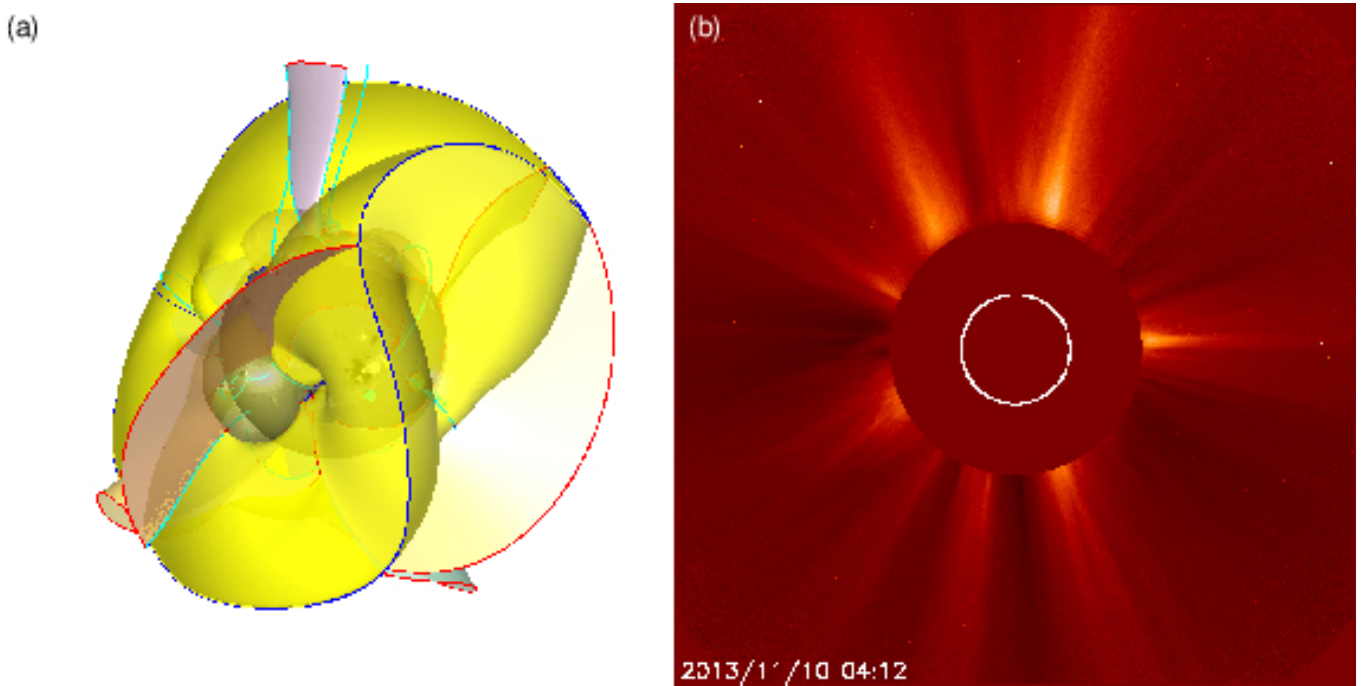


Figure 2. Comparison between the (a) topological skeleton and (b) LASCO C2 image as in Figure 1, but for SOL2013-11-10T05:14 (Event 48 in Table 1). The conical cyan pointer indicating the X-class flare location S14W13 is underneath the HCS curtain. Here, there are several LASCO streamers and it is more challenging to associate their positions with features in the PFSS model topology. Likewise, it is hard to anticipate the locations of LASCO streamers from the PFSS topology skeleton.

occur by looking only at the topological rendering, and it is correspondingly difficult to choose features in the topological rendering that match the LASCO streamers. Streamers and pseudostreamers are only evident when there is a significant amount of plasma density along the line of sight, and this suggests that the orientation of the HCS curtains may affect the presence or absence of streamers, especially if the HCS curtains are more face-on than edge-on. Figure 2(a) indicates that the HCS curtains for Event 48 are more folded and undulated, with portions being oriented face-on. As a consequence, for this particular case the comparison is deemed inconclusive.

2.2.2. Comparisons with Coronal Holes

The second sanity check relies on the association of dark regions in EUV images with open fields. The plasma along open fieldlines is too cool and too rarefied to emit in EUV wavelengths, and much of it is instead streaming upward to become the solar wind. Therefore, comparisons between the open-flux domains predicted by the PFSS model and the dark regions in EUV and X-ray imagery can be used to gauge how well the large-scale coronal magnetic field is represented by the PFSS models.

Such comparisons are imperfect, and a one-to-one correspondence between EUV-dark regions in the images and open-flux domains from the model is not expected (see Lowder et al. 2014, 2017 for recent comparisons). Several reasons probably account for these discrepancies: (1) Coronal holes may not indicate open flux; instead, this plasma may be located on long, closed fieldlines that connect faraway regions of opposite polarities. The plasma found on such long fieldlines is often not at the proper density or temperature to emit in EUV wavelengths, and thus remains dark. (2) The corona is optically thin, and as a result lines of sight passing through both closed and open fields will almost always appear bright. Such bright coronal structures may obscure open-field channels, especially away from disk center, and as a result open-flux regions will not appear dark in the EUV if there is not a direct line of sight into the channel. (3) The static upper boundary of the PFSS model only crudely approximates the dynamic environment present at the boundary between the magnetism-dominated corona and the plasma-dominated heliosphere. One consequence of this situation is that measurements of the *in situ* open flux at 1 AU do not match that predicted by the PFSS model (Linker et al. 2017). (4) The PFSS open-flux domains are large-scale features that span the full height of the model, and as a result may be affected by the lack of up-to-date surface magnetic fields at east-limb longitudes (as in the case discussed in Pevtsov et al. 2016). Structures in the eastern hemisphere may be ad-

versely affected when there is a significant amount of flux at or past the east limb that has not yet been assimilated into the surface-flux model that comprises the lower-boundary condition of the PFSS extrapolation.

Figure 3 illustrates the comparison between the modeled open flux and coronal holes for Event 11 (the same event shown in Figure 1). The image in Figure 3(a) shows a magnetogram for 2001 April 15 at about 0 UT, on which are overplotted the outlines of the photospheric footpoints of field lines that intersect R_{top} . Open fieldlines fan out from these contours, sometimes with significant expansion factors. The colors of the open-field contours in the figure indicate the polarity of the open flux. These open-field contours may be qualitatively compared with the darker regions of the full-Sun image from the 284Å channel observed by the Extreme ultraviolet Imaging Telescope (EIT; Delaboudinière et al. 1995) on SOHO, shown in Figure 3(b).

In the case shown in Figure 3, there is a fair amount of correspondence between many of the open-flux contours and the coronal holes, with the shapes of the darker features in the EIT image bearing resemblance to several of the shapes of the open-flux contours. In particular, the coronal hole and the PFSS open flux domain at the north pole have similar outlines. Similarly, the curved shape of open-flux region near the central meridian that spans the near-equatorial latitudes resembles the corresponding darker channels in the EUV image, though the degree to which they match is not as good for this equatorial coronal hole as in the polar coronal hole described earlier. This region of open flux is narrow, and brighter plasma associated with neighboring closed fields may be obscuring the full coronal hole. The same effect may be why the modeled open-flux extension in the southeast quadrant of Figure 3(a) has no noticeable coronal hole in the EUV image of Figure 3(b), although east-limb open-flux contours may also be affected by inaccuracies in the photospheric boundary condition.

Figure 4 shows the same comparison for Event 52. On this date, a PFSS open-flux region extends northward from the south polar region. At the top of this extension there is a ring of open flux that surrounds a closed-field domain. The comparison image from the 193Å channel of AIA also contains a dark coronal hole extending in the same direction as in the model, as well as some evidence that a circular channel of open flux might be present. Additionally, the coronal hole in the northeastern quadrant of the AIA image that appears to extend behind the limb matches well with the location of an open-flux region evident in the same location in the PFSS model.

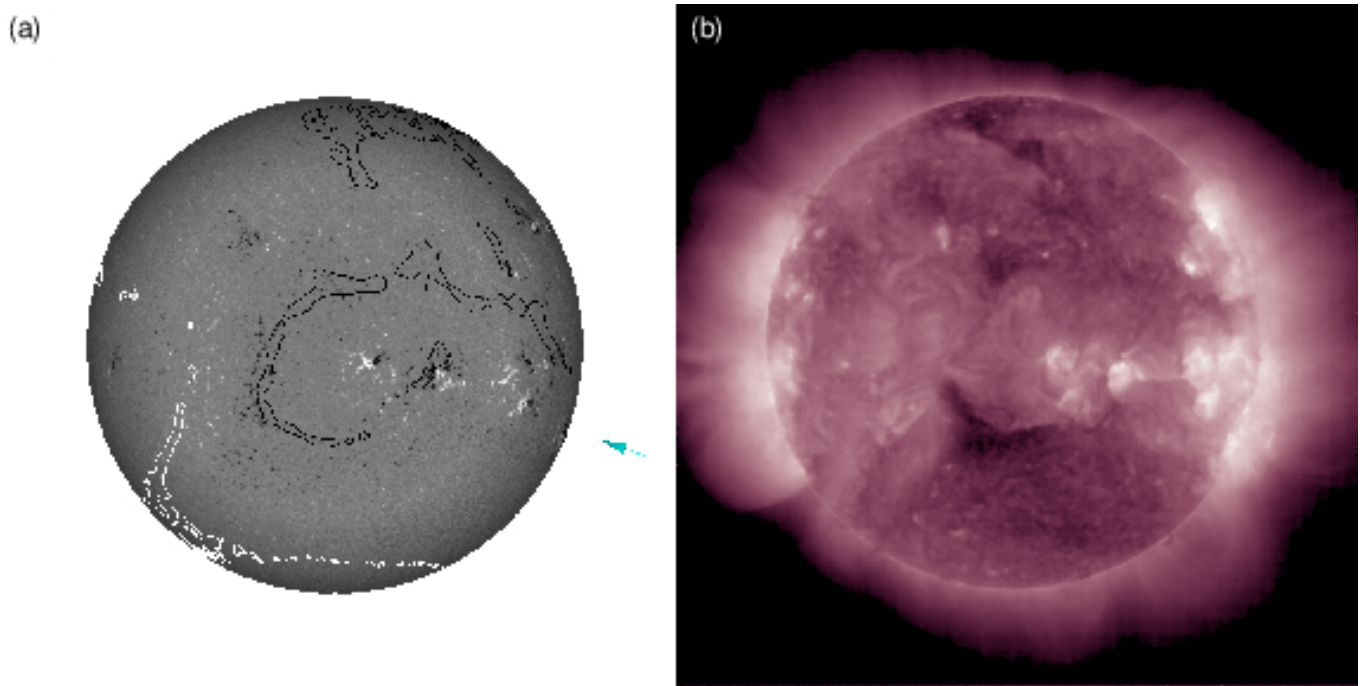


Figure 3. SOL2001-04-15T13:50 (Event 11 in Table 1) comparison: (a) Outlines of open flux from the PFSS model of 2001 April 15 at 12:04 UT overlaid on the nearest MDI line-of-sight magnetogram and (b) the corresponding full-Sun image from the 284Å channel of EIT. The conical cyan pointer in panel (a) indicates the location of the X-class flare at S20W85. The open-flux contours from the PFSS model match the coronal holes observed by EIT reasonably well, in this case.

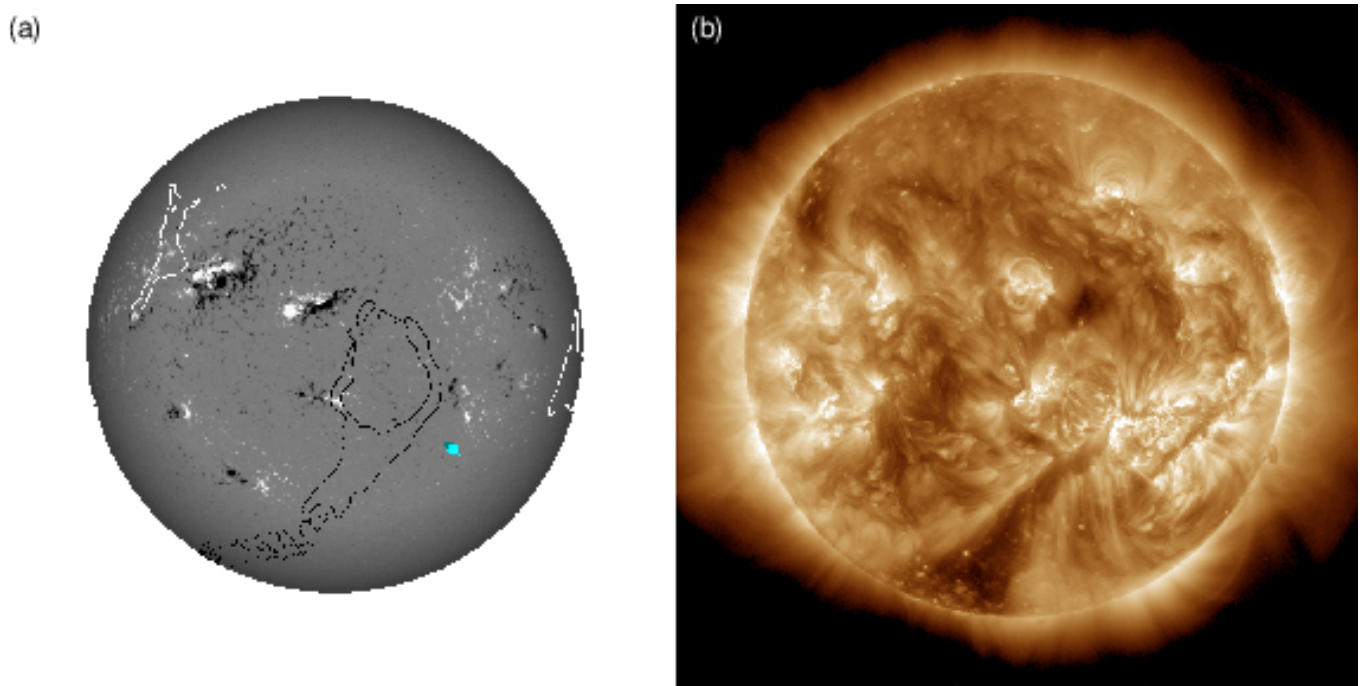


Figure 4. As in Figure 3, a comparison for SOL2014-12-20T00:28 (Event 52 in Table 1) between the (a) outlines of open flux from the PFSS model and (b) the corresponding full-Sun image from the 193Å channel of AIA. The conical cyan pointer in panel (a) indicates the location of the X-class flare at S21W24. The open-flux contours from the PFSS model match the coronal holes observed by AIA reasonably well, in this case.

Table 1. Sample of flaring active regions

Event	SOL (flare peak time) ^a	flare class ^b	NOAA AR ^c	Location ^d	Eruptive? ^e	Access? ^f	Notes
1	SOL1996-07-09T09:12	X2.6	7978	S10W30	Yes	No	
2	SOL1997-11-04T05:58	X2.1	8100	S14W33	Yes	Yes	
3	SOL1998-05-02T13:42	X1.1	8210	S15W15	Yes	Yes	<i>g</i>
4	SOL1999-08-28T18:05	X1.1	8674	S26W14	Yes	No	<i>h</i>
5	SOL1999-11-27T12:12	X1.4	8771	S15W68	No	No	
6	SOL2000-11-24T15:13	X2.3	9236	N22W7	Yes	Yes	
7	SOL2000-11-25T18:44	X1.9	"	N20W23	Yes	Yes	
8	SOL2000-11-26T16:48	X4.0	"	N18W38	Yes	Yes	
9	SOL2001-03-29T10:15	X1.7	9402	N20W19	Yes	Yes	<i>g</i>
10	SOL2001-04-10T05:26	X2.3	9415	S23W9	Yes	Yes	
11	SOL2001-04-15T13:50	X14.	"	S20W85	Yes	Yes	
12	SOL2001-10-19T16:30	X1.6	9661	N15W29	Yes	No	<i>h</i>
13	SOL2001-10-25T15:02	X1.3	9672	S16W21	Yes	No	<i>h</i>
14	SOL2001-11-04T16:20	X1.0	9684	N6W18	Yes	No	
15	SOL2002-07-18T07:44	X1.8	10030	N19W30	Yes	Yes	
16	SOL2002-08-21T05:34	X1.0	10069	S12W51	Yes	Yes	<i>i</i>
17	SOL2003-03-17T19:05	X1.5	10314	S14W39	Yes	No	
18	SOL2003-03-18T12:08	X1.5	"	S15W46	Yes	No	<i>j</i>
19	SOL2003-05-27T23:07	X1.3	10365	S7W17	Yes	No	
20	SOL2003-05-29T01:05	X1.2	"	S6W37	Yes	No	
21	SOL2003-10-26T18:19	X1.2	10484	N2W38	Yes	Yes	
22	SOL2003-10-29T20:49	X10.	10486	S15W2	Yes	Yes	
23	SOL2003-11-02T17:25	X8.3	"	S14W56	Yes	Yes	
24	SOL2003-11-03T01:30	X2.7	10488	N10W83	Yes	No	
25	SOL2003-11-03T09:55	X3.9	"	N8W77	Yes	No	
26	SOL2003-11-04T19:50	X28.	10486	S19W83	Yes	Yes	
27	SOL2004-02-26T02:03	X1.1	10564	N14W15	No	No	<i>j</i>
28	SOL2004-08-13T18:12	X1.0	10656	S13W24	Yes	Yes	
29	SOL2004-08-18T17:40	X1.8	"	S14W90	Yes	Yes	
30	SOL2004-10-30T11:46	X1.2	10691	N13W25	Yes	Yes	
31	SOL2004-11-07T16:06	X2.0	10696	N9W17	Yes	No	<i>j</i>
32	SOL2004-11-10T02:13	X2.5	"	N9W49	Yes	No	
33	SOL2005-01-15T23:02	X2.6	10720	N14W8	Yes	No	
34	SOL2005-01-17T09:52	X3.8	"	N15W25	Yes	Yes	
35	SOL2005-01-19T08:22	X1.3	"	N15W51	Yes	Yes	
36	SOL2005-01-20T07:01	X7.1	"	N14W61	Yes	Yes	
37	SOL2005-07-14T10:55	X1.2	10786	N11W90	Yes	No	<i>h</i>
38	SOL2005-09-15T08:38	X1.1	10808	S12W14	No	Yes	<i>i</i>
39	SOL2006-12-13T02:40	X3.4	10930	S6W23	Yes	Yes	
40	SOL2006-12-14T22:15	X1.5	"	S6W46	Yes	Yes	
41	SOL2011-02-15T01:56	X2.2	11158	S20W10	Yes	No	<i>j</i>
42	SOL2011-03-09T23:23	X1.5	11166	N8W11	No	No	
43	SOL2011-08-09T08:05	X6.9	11263	N14W69	Yes	No	
44	SOL2011-09-06T22:20	X2.1	11283	N14W18	Yes	Yes	
45	SOL2011-09-07T22:38	X1.8	"	N14W31	Yes	Yes	
46	SOL2012-07-12T16:49	X1.4	11520	S13W3	Yes	No	<i>h</i>
47	SOL2013-10-28T02:03	X1.0	11875	N4W66	Yes	Yes	
48	SOL2013-11-10T05:14	X1.1	11890	S14W13	Yes	No	<i>h</i>
49	SOL2014-03-29T17:48	X1.0	12017	N10W32	Yes	Yes	<i>i</i>
50	SOL2014-10-26T10:56	X2.0	12192	S14W37	No	No	<i>h</i>
51	SOL2014-10-27T14:47	X2.0	"	S16W56	No	No	
52	SOL2014-12-20T00:28	X1.8	12242	S21W24	Yes	Yes	

Table 1 continued

Table 1 (continued)

Event	SOL (flare peak time) ^a	flare class ^b	NOAA AR ^c	Location ^d	Eruptive? ^e	Access? ^f	Notes
53	SOL2017-09-06T09:10	X2.2	12673	S8W32	Yes	Yes	<i>g</i>
54	SOL2017-09-06T12:02	X9.3	"	S9W34	Yes	Yes	<i>g</i>
55	SOL2017-09-07T14:36	X1.3	"	S8W48	Yes	Yes	
56	SOL2017-09-10T16:06	X8.2	"	S8W88	Yes	Yes	

^aSolar Object Locator (SOL) of time of peak flare emission from the *GOES* flare catalog

^bFlare class from the *GOES* flare catalog

^cActive region number assigned by NOAA

^dFlare location from the *GOES* flare catalog

^eIs there an eruption in LASCO C2 and/or C3 data following the time of the flare peak?

^fDoes the PFSS model imply access to open field from an upward-directed eruption centered on the flare location?

^gAccess to open fields is provided via a narrow channel located between separatrix surfaces. This channel extends either into or through the AR and encompasses the flare site, as in the example shown in Figure 5.

^hThere is a significant volume of closed field above the flare site that likely blocks access to open fields for any flux structure that may accelerate upward, even though the flare location is laterally adjacent to open flux. An example of this phenomenon is shown in Figure 2.

ⁱThe flare is sited near a (small, often) region of open field that significantly expands with height, creating a funnel- or fan-shaped open-flux domain that overlies any upwardly mobile flux structure located at the flare site. An example of this phenomenon is shown in Figure 6.

^jThe location of the flare is underneath a separatrix dome associated with a null point located in the coronal volume, according to the PFSS model.

3. RESULTS AND DISCUSSION

The final sample of events comprises 56 flares occurring within 37 ARs, as listed in Table 1 and in the online materials associated with this article (<http://www.lmsal.com/forecast/DB2018.html>). Each flare in the sample is classified as either eruptive or non-eruptive, based on whether a CME is observed in LASCO data. We made use of the LASCO CME catalog³ to determine whether the flares have an associated CME. Examining LASCO C2 and C3 running difference movies is particularly helpful for this purpose, and the LASCO CME catalog has conveniently provided a useful movie-making tool that synchronizes LASCO C2 and C3 running difference movies with GOES X-ray light curves. In the online materials, a link to such a synchronized movie is provided for each of the 56 events.

We also characterize each event based on whether there is access to open fields from the location of the flare. More specifically, we consider in a qualitative manner how likely it is that a rising flux structure located at the flare site would encounter open fields as it moves radially outward through the PFSS model. In some cases, this is easily judged as, for example, when the source AR is permeated by open fields, or when the source AR is centered underneath the helmet surface (and is thus obviously buried beneath a significant amount of closed field). Many cases are more ambiguous, and thus making the determination is more subjective.

Narrow channels of open flux are a common feature in PFSS coronal field models, and are usually nestled either between separatrix surfaces that divide different topological domains of the magnetic field or between tight folds in the HCS curtain. The fields emanating from these channels often have high expansion factors, especially in the direction perpendicular to the channel orientation, and are believed to play a key role in the formation of the slow solar wind (Antiochos et al. 2007, 2011; Titov et al. 2011). In the context of this study, narrow channels that pass in or through a flaring AR provide a pathway by which plasma and fields may be readily ejected into interplanetary space, even though the flare site may not be located precisely above the photospheric open-field footprint. Because of their small photospheric area, such open-field channels are sometimes difficult to identify in EUV imagery.

As an example of this phenomenon, Figure 5 illustrates a narrow channel encroaching upon the trailing polarity of AR 12673, which produced the series of recent X-class flares in September 2017. Although the closest region of photospheric open flux is not directly underneath the flare site, we consider this region to have access to open fields because of how quickly with height this nearby open flux splay out. A variant of this effect involves open-flux domains with even smaller photospheric areas that map down to strong flux, such as for SOL2002-08-21T05:34 shown in Figure 6. As with AR 12673, the open fields above AR 10069 map down to a small, isolated region on the photosphere in the trailing polarity of the flaring AR.

³ At the time of this writing, the LASCO CME catalog can be found at https://cdaw.gsfc.nasa.gov/CME_list/index.html.

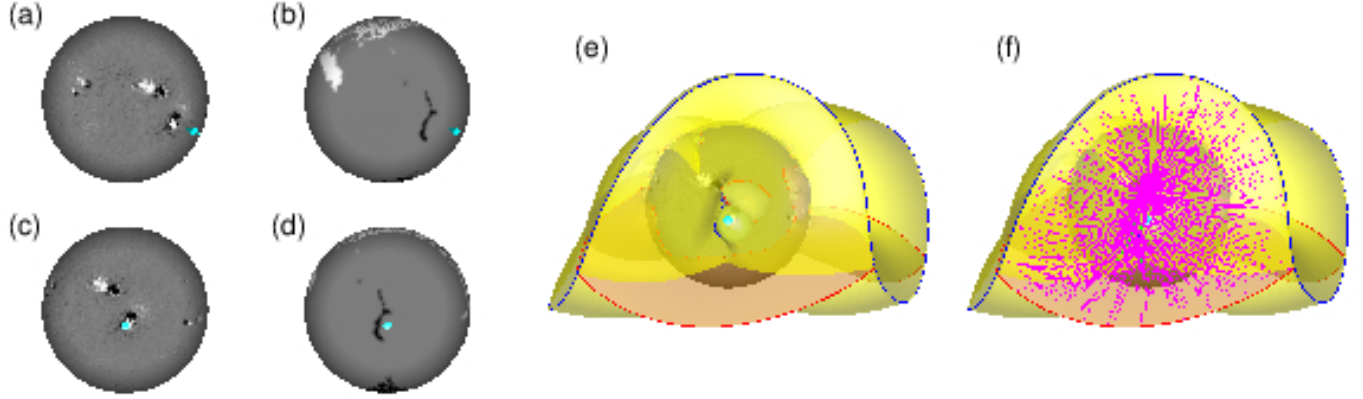


Figure 5. A narrow channel of open flux is associated with SOL2017-09-06T09:10 and SOL2017-09-06T12:02 (Events 53 and 54 in Table 1). Panels (a) and (b) show the photospheric magnetic fields and the photospheric open-flux regions from the PFSS extrapolation, respectively, as viewed from the Earth-Sun line, with color indicative of polarity. Panels (c) and (d) are the same as panels (a) and (b), except that the models have been rotated so that the flare longitude is centered. Panels (e) and (f) show the topological separatrix surfaces as rendered on the magnetic map shown in panel (c), with the HCS curtain (colored yellow) dominating the image. A separatrix curtain (colored orange) in the southern hemisphere divides the negative open flux into separate domains. Near disk center lies a narrow channel of open-flux that passes close to the flaring AR. Field lines emanating from this particular domain, shown in panel (f), are seen to have high expansion factors. In all panels, the conical cyan pointer indicates the location of the X-class flares.

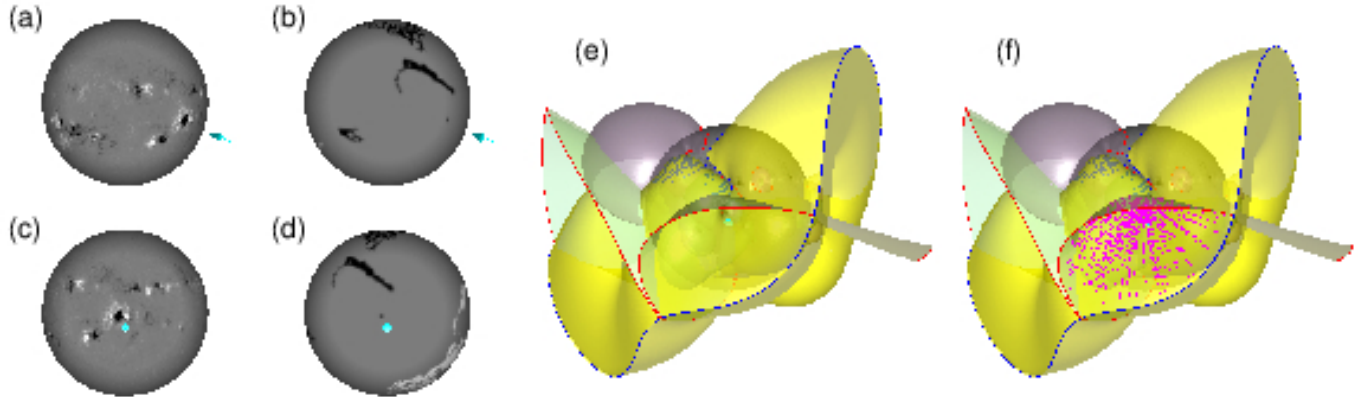


Figure 6. A small spot of open flux is located near SOL2002-08-21T05:34 (Event 16 in Table 1). As in Figure 5, panels (a)–(d) show the photospheric magnetic fields and the photospheric open-flux regions from different perspectives, and panels (e) and (f) show the topological separatrix surfaces from the coronal field model. A small spot of open flux is located in the trailing polarity of the AR associated with the event. Open flux extends upward from this spot to occupy the volume between one of the separatrix curtains and the yellow HCS curtain. In all panels, the conical cyan pointer indicates the location of the X-class flare.

Table 2. Contingency Table

		Eruptive?	
		Yes	No
Access?	Yes	$n_{eo} = 30$	$n_{no} = 1$
	No	$n_{ec} = 20$	$n_{nc} = 5$

Table 2 is a contingency table that summarizes the number of events that fall into each of the defined categories. The tabulation shows that of the 50 X-class flares associated with a CME, 30 of these (60%) occurred in locations judged as having access to open flux. There are only 6 non-eruptive X-class flares in the sample, and 5 of these were sited in places with significant overlying closed fields. We estimate the rate at which X-class flares with access to open flux are eruptive as 0.97 (30/31) compared with 0.80 (20/25) for X-class flares without access to open flux. These estimates are, however, based on a small number (6) of non-eruptive flares.

To test how robust the results are, we computed the Bayes factor K (e.g., Kass & Raftery 1995) comparing a model in which the rate at which X-class flares are eruptive is independent of access to open field with a model in which access to open field results in a different rate of eruptions (see Appendix A). Depending on the choice of priors, the Bayes factor is in the range $0.12 \leq K \leq 0.74$, which indicates that there is weak to moderate evidence to support that access to open field influences whether an X-flare is eruptive.

4. CONCLUSIONS

We conclude that X-class flares are more likely to be eruptive when they occur in locations with access to open flux. The evidence to support this, however, is statistically sensitive to the small number of non-eruptive X-class flares in the sample. Of the 31 X-class flares that were judged to originate in locations with access to open field, all except one (SOL2005-09-15T08:38) were eruptive. The sample also contains 25 X-class flares located far away from open fields,

of which 20 were eruptive and 5 were non-eruptive. Access to open field is therefore neither a necessary nor a sufficient condition for a flare to result in an eruption.

To more definitively conclude that access to open field influences whether an X-class flare is likely to be eruptive, a larger sample of non-eruptive flares is needed. This sample might be accomplished, for example, by relaxing the requirement used here that the flare be sited west of central meridian, though by doing this there is a concern that the open-field regions on the Sun may not be accurately determined by the PFSS model. This would probably increase the risk of a flare location being classified as having access (or non-access) to open flux in a way that is difficult to quantify.

Alternatively, the sample might be expanded to include flares of smaller magnitude. While including such smaller magnitude events would result in better statistics, it would also raise the question of whether non-eruptive flares are such because they lack the energy to fully form a CME or whether they are non-eruptive due to a lack of access to open field. In reality, these two factors (energy deposited and access to open field) are likely linked, given that a very energetic event may be able to push through a small amount of closed field to access open field that would otherwise be inaccessible for less energetic cases.

In this investigation, we focused on whether an X-class flare was sited in a location with access to open fields. However, the topology of the coronal magnetic field is complex, and contains narrow channels of open flux wedged between closed domains of connectivity. Closed fields may lie underneath separatrix domes associated with coronal null point, or they may be found under the large helmet surface(s) that often wrap around the Sun. With a larger sample size, the specific topologies associated with both eruptive and non-eruptive flares may become more apparent.

This material is based upon work supported by the National Science Foundation under Grant No. 1357018 to Lockheed Martin. G.B. also acknowledges support from NASA under award number NNX14AD45G.

APPENDIX

A. STATISTICAL CONSIDERATIONS

To quantitatively evaluate whether access to open field influences whether an X-flare is eruptive, consider the following two models. In the first model, M_1 , access to open field does not play a role in determining whether an X-flare is eruptive. In the second model, M_2 , X-class flares are eruptive at a different rate when there is access to open field compared to when there are no nearby open fields. To determine which of these models is more likely, we compute the Bayes factor (odds ratio), which is a statistic that compares the likelihood of getting the observed data from each of the models. More explicitly, the two models for the observations are:

M_1 : The probability that an X-flare will produce an eruption, p_e , is independent of the proximity to open field.

M_2 : The probability that an X-flare will produce an eruption depends on whether there is access to open field at the flare site, where p_o is the probability that the site of the X-class flare is located near access to open field, and where p_c is the probability that an X-flare occurs in a location without any nearby open field.

The data used to evaluate the likelihood of each of these models is summarized in a contingency table D (i.e., as shown in Table 2), whose elements are:

n_{eo} : the number of eruptive X-class flares with access to open field.

n_{no} : the number of non-eruptive X-class flares with access to open field.

n_{ec} : the number of eruptive X-class flares under closed field.

n_{nc} : the number of non-eruptive X-class flares under closed field.

The probability of the observed contingency table D resulting from each of the models M_i , assuming binomial random variables, can now be calculated. For M_1 , the probability of getting D , for a given eruption probability p_e , is

$$Pr(D|p_e, M_1) = \frac{n_o!n_c!}{n_{eo}!n_{no}!n_{ec}!n_{nc}!} p_e^{n_e} (1 - p_e)^{n_n}, \quad (\text{A1})$$

where n_e is the number of eruptive X-class flares, n_n is the number of non-eruptive X-class flares, n_o is the number of X-class flares from ARs with access to open field, and n_c is the number of X-class flares from ARs under closed field. Marginalizing over p_e results in the following probability of the data, assuming a uniform prior on p_e given model M_1 ($Pr(p_e|M_1) = 1$ for $0 \leq p_e \leq 1$):

$$Pr(D|M_1) = \int_0^1 dp_e Pr(p_e|M_1) Pr(D|p_e, M_1) \quad (\text{A2})$$

$$= \frac{n_o!n_c!}{n_{eo}!n_{no}!n_{ec}!n_{nc}!} \frac{n_e!n_n!}{(n_e + n_n + 1)!}. \quad (\text{A3})$$

For M_2 , the probability of getting D , given probabilities p_o and p_c , is

$$Pr(D|p_o, p_c, M_2) = \left[\frac{n_o!}{n_{eo}!n_{no}!} p_o^{n_{eo}} (1 - p_o)^{n_{no}} \right] \left[\frac{n_c!}{n_{ec}!n_{nc}!} p_c^{n_{ec}} (1 - p_c)^{n_{nc}} \right]. \quad (\text{A4})$$

Marginalizing over p_o and p_c results in the probability of the data, assuming uniform priors on p_o and p_c given model M_2 ($Pr(p_o|M_2) = 1$ for $0 \leq p_o \leq 1$, $Pr(p_c|M_2) = 1$ for $0 \leq p_c \leq 1$):

$$Pr(D|M_2) = \int_0^1 dp_o \int_0^1 dp_c Pr(p_o|M_2) Pr(p_c|M_2) Pr(D|p_o, p_c, M_2) \quad (\text{A5})$$

$$= \frac{n_o!n_c!}{(n_o + 1)!(n_c + 1)!}. \quad (\text{A6})$$

Given $Pr(D|M_1)$ and $Pr(D|M_2)$, the Bayes factor K is therefore given by (e.g., Kass & Raftery 1995):

$$K = \frac{Pr(D|M_1)}{Pr(D|M_2)} \quad (\text{A7})$$

$$= \frac{n_e!n_n!(n_o + 1)!(n_c + 1)!}{n_{eo}!n_{no}!n_{ec}!n_{nc}!(n_e + n_n + 1)!}, \quad (\text{A8})$$

where a value of $K = 1$ indicates that both models are equally likely to produce the observed contingency table, i.e., neither model is more likely than the other with the choice of an uninformative prior (see, e.g., section 3.2 of Kass & Raftery 1995, for the interpretation of the Bayes factor). For the values given in Table 2, the Bayes factor is $K = 0.74$.

To determine how sensitive the result is to the choice of priors, we repeat this analysis using a delta function at the Maximum Likelihood Estimate for the values of p_* for each model. Marginalizing over the fraction p_e to get the probability of the data for model M_1 with $Pr(p_e|M_1) = \delta(p_e - n_e/(n_e + n_n))$ gives

$$Pr(D|M_1) = \int_0^1 dp_e Pr(p_e|M_1) Pr(D|p_e, M_1) \quad (\text{A9})$$

$$= \frac{n_o!n_c!}{n_{eo}!n_{no}!n_{ec}!n_{nc}!} \frac{n_e^{n_e} n_n^{n_n}}{(n_e + n_n)^{n_e + n_n}}. \quad (\text{A10})$$

For model M_2 , marginalizing over the fractions p_o and p_c to get the probability of the data for model M_2 with $Pr(p_o|M_1) = \delta(p_o - n_{eo}/n_o)$ and $Pr(p_c|M_1) = \delta(p_c - n_{ec}/n_c)$ gives

$$Pr(D|M_2) = \int_0^1 dp_o \int_0^1 dp_c Pr(p_o|M_2) Pr(p_c|M_2) Pr(D|p_o, p_c, M_2) \quad (A11)$$

$$= \frac{n_o! n_c!}{n_{eo}! n_{no}! n_{ec}! n_{nc}!} \frac{n_{eo}^{n_{eo}} n_{no}^{n_{no}}}{n_o^{n_o}} \frac{n_{ec}^{n_{ec}} n_{nc}^{n_{nc}}}{n_c^{n_c}}. \quad (A12)$$

Thus, the Bayes factor for these priors is given by

$$K = \frac{Pr(D|M_1)}{Pr(D|M_2)} \quad (A13)$$

$$= \frac{n_e^{n_e} n_n^{n_n} n_o^{n_o} n_c^{n_c}}{(n_e + n_n)^{n_e + n_n} n_{eo}^{n_{eo}} n_{no}^{n_{no}} n_{ec}^{n_{ec}} n_{nc}^{n_{nc}}}, \quad (A14)$$

which has a value $K = 0.12$ for the values given in Table 2. This value indicates that model M_2 is much more likely.

The conclusion clearly depends on the choice of priors, in part because of the extremely small number of non-eruptive flares. The two sets of priors chosen represent the extremes, and thus the real Bayes factor should lie between these two.

Facility: GOES/XRS, SDO/AIA, SDO/HMI, SOHO/EIT, SOHO/LASCO, SOHO/MDI

REFERENCES

Antiochos, S. K., DeVore, C. R., Karpen, J. T., & Mikić, Z. 2007, *ApJ*, 671, 936

Antiochos, S. K., Mikić, Z., Titov, V. S., Lionello, R., & Linker, J. A. 2011, *ApJ*, 731, 112

Bohlin, J. D. 1970, *SoPh*, 12, 240

Brueckner, G. E., Howard, R. A., Koomen, M. J., Korendyke, C. M., Michels, D. J., Moses, J. D., Socker, D. G., Dere, K. P., Lamy, P. L., Llebaria, A., Bout, M. V., Schwenn, R., Simnett, G. M., Bedford, D. K., & Eyles, C. J. 1995, *SoPh*, 162, 357

Delaboudinière, J.-P., Artzner, G. E., Brunaud, J., Gabriel, A. H., Hochedez, J. F., Millier, F., Song, X. Y., Au, B., Dere, K. P., Howard, R. A., Kreplin, R., Michels, D. J., Moses, J. D., Defise, J. M., Jamar, C., Rochus, P., Chauvineau, J. P., Marioge, J. P., Catura, R. C., Lemen, J. R., Shing, L., Stern, R. A., Gurman, J. B., Neupert, W. M., Maucherat, A., Clette, F., Cugnon, P., & van Dessel, E. L. 1995, *SoPh*, 162, 291

Edwards, S. J., Parnell, C. E., Harra, L. K., Culhane, J. L., & Brooks, D. H. 2016, *SoPh*, 291, 117

Emslie, A. G., Dennis, B. R., Shih, A. Y., Chamberlin, P. C., Mewaldt, R. A., Moore, C. S., Share, G. H., Vourlidas, A., & Welsch, B. T. 2012, *ApJ*, 759, 71

Freed, M. S., Longcope, D. W., & McKenzie, D. E. 2015, *SoPh*, 290, 467

Haynes, A. L., & Parnell, C. E. 2007, *Phys. Plasmas*, 14, 082107

—. 2010, *Phys. Plasmas*, 17, 092903

Hurlburt, N., Cheung, M., Schrijver, C., Chang, L., Freeland, S., Green, S., Heck, C., Jaffey, A., Kobashi, A., Schiff, D., Serafin, J., Seguin, R., Slater, G., Soman, A., & Timmons, R. 2012, *SoPh*, 275, 67

Janvier, M. 2017, *J. Plasma Phys.*, 83, 535830101

Jin, M., Schrijver, C. J., Cheung, M. C. M., DeRosa, M. L., Nitta, N. V., & Title, A. M. 2016, *ApJ*, 820, 16

Kass, R. E., & Raftery, A. E. 1995, *J. Am. Stat. Assoc.*, 90, 773

Lemen, J. R., Title, A. M., Akin, D. J., Boerner, P. F., Chou, C., Drake, J. F., Duncan, D. W., Edwards, C. G., Friedlaender, F. M., Heyman, G. F., Hurlburt, N. E., Katz, N. L., Kushner, G. D., Levay, M., Lindgren, R. W., Mathur, D. P., McFeaters, E. L., Mitchell, S., Rehse, R. A., Schrijver, C. J., Springer, L. A., Stern, R. A., Tarbell, T. D., Wuelser, J.-P., Wolfson, C. J., Yanari, C., Bookbinder, J. A., Cheimets, P. N., Caldwell, D., Deluca, E. E., Gates, R., Golub, L., Park, S., Podgorski, W. A., Bush, R. I., Scherrer, P. H., Gummin, M. A., Smith, P., Auker, G., Jerram, P., Pool, P., Soufli, R., Windt, D. L., Beardsley, S., Clapp, M., Lang, J., & Waltham, N. 2012, *SoPh*, 275, 17

Lin, H., Kuhn, J. R., & Coulter, R. 2004, *ApJL*, 613, L177

Linker, J. A., Caplan, R. M., Downs, C., Riley, P., Mikic, Z., Lionello, R., Henney, C. J., Arge, C. N., Liu, Y., Derosa, M. L., Yeates, A., & Owens, M. J. 2017, *ApJ*, 848, 70

Liu, R., Titov, V. S., Gou, T., Wang, Y., Liu, K., & Wang, H. 2014, *ApJ*, 790, 8

Lowder, C., Qiu, J., & Leamon, R. 2017, *SoPh*, 292, 18

Lowder, C., Qiu, J., Leamon, R., & Liu, Y. 2014, *ApJ*, 783, 142

Nitta, N. V., & DeRosa, M. L. 2008, *ApJL*, 673, L207

Pevtsov, A. A., Bertello, L., MacNeice, P., & Petrie, G. 2016, *Space Weather*, 14, 1026

Platten, S. J., Parnell, C. E., Haynes, A. L., Priest, E. R., & Mackay, D. H. 2014, *A&A*, 565, A44

Pontin, D., Galsgaard, K., & Démoulin, P. 2016, *SoPh*, 291, 1739

Pontin, D. I. 2012, *Phil. Trans. R. Soc. London, Ser. A*, 370, 3169

Pontin, D. I., & Wyper, P. F. 2015, *ApJ*, 805, 39

Régnier, S. 2012, *SoPh*, 277, 131

Schatten, K. H., Wilcox, J. M., & Ness, N. F. 1969, *SoPh*, 6, 442

Scherrer, P. H., Bogart, R. S., Bush, R. I., Hoeksema, J. T., Kosovichev, A. G., Schou, J., Rosenberg, W., Springer, L., Tarbell, T. D., Title, A., Wolfson, C. J., Zayer, I., & MDI Engineering Team. 1995, *SoPh*, 162, 129

Schou, J., Scherrer, P. H., Bush, R. I., Wachter, R., Couvidat, S., Rabbelo-Soares, M. C., Bogart, R. S., Hoeksema, J. T., Liu, Y., Duvall, T. L., Akin, D. J., Allard, B. A., Miles, J. W., Rairden, R., Shine, R. A., Tarbell, T. D., Title, A. M., Wolfson, C. J., Elmore, D. F., Norton, A. A., & Tomczyk, S. 2012, *SoPh*, 275, 229

Schrijver, C. J., & DeRosa, M. L. 2003, *SoPh*, 212, 165

Schrijver, C. J., DeRosa, M. L., & Title, A. M. 2010, *ApJ*, 719, 1083

Schrijver, C. J., & Title, A. M. 2011, *J. Geophys. Res.*, 116, A04108

Sun, X., Bobra, M. G., Hoeksema, J. T., Liu, Y., Li, Y., Shen, C., Couvidat, S., Norton, A. A., & Fisher, G. H. 2015, *ApJL*, 804, L28

Titov, V. S., Mikić, Z., Linker, J. A., Lionello, R., & Antiochos, S. K. 2011, *ApJ*, 731, 111

Toriumi, S., Schrijver, C. J., Harra, L. K., Hudson, H., & Nagashima, K. 2017, *ApJ*, 834, 56

Toriumi, S., & Takasao, S. 2017, *ApJ*, 850, 39

Wang, D., Liu, R., Wang, Y., Liu, K., Chen, J., Liu, J., Zhou, Z., & Zhang, M. 2017, *ApJL*, 843, L9

Wang, Y., Biersteker, J. B., Sheeley, Jr., N. R., Koutchmy, S., Mouette, J., & Druckmüller, M. 2007a, *ApJ*, 660, 882

Wang, Y.-M., Sheeley, Jr., N. R., & Rich, N. B. 2007b, *ApJ*, 658, 1340

Zhao, J., Gilchrist, S. A., Aulanier, G., Schmieder, B., Pariat, E., & Li, H. 2016, *ApJ*, 823, 62

Zhao, J., Li, H., Pariat, E., Schmieder, B., Guo, Y., & Wiegmann, T. 2014, *ApJ*, 787, 88